J Eng Math (2007) 62:133–148
DOI 10.1007/s10665-007-9183-1

Axisymmetric waves in electrohydrodynamic flows

Scott Grandison · Jean-Marc Vanden-Broeck · Demetrios T. Papageorgiou · Touvia Miloh · Boaz Spivak

Received: 11 October 2006 / Accepted: 6 August 2007 / Published online: 12 September 2007

Abstract The formation of nonlinear axisymmetric waves on inviscid irrotational liquid jets in the presence of radial electric fields is considered. Gravity is neglected but surface tension is considered. Electrohydrodynamic waves of arbitrary amplitude and wavelength are computed using finite-difference methods. Particular attention is paid to nonlinear traveling waves. In the first class of problems, an electric field generated by placing the liquid jet inside a hollow cylindrical electrode held at constant voltage, its axis coinciding with that of the jet, is studied. The jet is assumed to be a perfect conductor whose free surface is stressed by the electric field acting in the hydrodynamically passive annulus. In the second class of problems, the annular gas is a perfect conductor that transmits a constant voltage onto the liquid/gas surface. The liquid axisymmetrically wets a constant-radius cylindrical rod electrode placed coaxially with respect to the hollow outer electrode, and held at a different constant voltage. The fluid dynamics and electrostatics need to be addressed simultaneously in the inner region. Axisymmetric interfacial waves influenced by surface tension and electrical stresses are computed in both cases. The computations are capable of following highly nonlinear solutions and predict, for certain parameter values, the onset of interface pinching accompanied with the formation of toroidal bubbles. For given wave amplitudes, the results suggest that, for the former case, the electric field delays bubble formation and reduces wave steepness, while for the latter case the electric field promotes bubble formation, all other parameters being equal.

Keywords Capillary waves · Cylindrical jet · Electric field

S. Grandison · J.-M. Vanden-Broeck
School of Mathematics, University of East Anglia, Norwich NR4 7TJ, UK

D. T. Papageorgiou (✉)
Department of Mathematical Sciences, New Jersey Institute of Technology, University Heights, Newark, NJ 07102, USA
e-mail: depapa@oak.njit.edu

T. Miloh
Department of Fluid Mechanics and Mass Transfer, Tel Aviv University, Ramat Aviv 69978, Israel

B. Spivak
Department of Electrical and Electronics Engineering, Holon Institute of Technology, Holon, Israel

1 Introduction

We consider a three-dimensional axisymmetric fluid jet which initially has uniform radius and is surrounded by a second fluid. We assume that the effects of gravity are negligible, a condition which is satisfied when the Bond number, $\rho g R^2/\sigma$, where ρ is the fluid density, g the acceleration due to gravity, R the undisturbed jet radius and σ the surface-tension coefficient, is small. This condition can be expected to hold for a thin jet and/or a large surface tension. An electric field driven by a constant potential difference acts in the radial direction. For nonlinear interfacial deformations we must solve for the hydrodynamics and the voltage potentials both inside and outside of the jet. The fluid motion and the electric field are coupled through the Maxwell stresses which modify the hydrodynamic stresses at the interface; see [1, Chapt. 6]. This constitutes a nonlinear problem which, in general, must be addressed numerically. We commence our study of the free-boundary problem by considering traveling-wave solutions with arbitrary amplitude and wavelength. We will consider two particular cases, one where the inner fluid is a perfect conductor and the outer fluid is a hydrodynamically passive dielectric, and second where the outer fluid is a perfect conductor and the inner fluid is a hydrodynamically passive dielectric. In the second case a rod electrode placed on the axis of symmetry is used to drive a radial electric field.

Wave formation on liquid layers in the presence of surface tension has been the subject of numerous investigations. Crapper [2] studied two-dimensional capillary waves in deep water and found a class of exact traveling-wave solutions for which the interface can be a single or multi-valued function. When gravity is also present, exact solutions are not possible. Gravity–capillary waves in irrotational flows have been computed numerically by a number of authors including Schwartz and Vanden-Broeck [3], Chen and Saffman [4], Hogan [5], Hunter and Vanden-Broeck [6] and Grandison and Vanden-Broeck [7].

Vanden-Broeck et al. [8] formulated a finite-difference scheme for calculating the location of the free surface of an axisymmetric jet. They calculated fully nonlinear solutions and demonstrated that there is a two-parameter family of solutions for axisymmetric jets. They also presented results which suggest that the waves ultimately reach a limiting configuration with a trapped bubble at the troughs, although they were unable to compute these limiting solutions. Subsequently Osborne and Forbes [9] presented a boundary-integral formulation and produced equivalent results, stating, however, that their scheme was more efficient than that of [8]. In this work we present a formulation that is an extension of the techniques used in [8].

There are a number of different applications that motivate this study. Examples include coating and cooling, where liquid films are used to enhance mass or heat transfer. Liquid jets and fluid-sheet problems have applications in printing, particle sorting, fuel injection and fibre formation. There are other applications such as film flows, the use of electric fields to modify stability properties of flows and using electric fields in fluid management of microfluidic devices.

There have been many studies on the stability of liquid jets in the presence of electric fields. Burcham and Saville [10] and Ramos et al. [11] show experimentally that axial electric fields tend to stabilize capillary-driven instabilities and enable longer stable bridges to emerge. In the case of inviscid liquids and axial electric fields, the reader is referred to the liquid-bridge boundary-integral computations reported in [12] and references therein. Linear oscillations in such regimes have been studied theoretically by Pelekasis et al. [13]. It was shown that the axial electric field stabilizes capillary instability, thus allowing longer bridges to maintain their integrity rather than evolve to pinching and drop formation. When radial electric fields act, the modification of the pressure due to the Maxwell stresses is different and the jet can be stabilized or destabilized, depending on the geometry. The classical linear problem has been solved by Basset [14], Schneider et al. [15], Neukermans [16] and more recently by Artana et al. [17,18] for absolute/convective studies. A boundary-element time-dependent computation of a perfectly conducting inviscid liquid jet in a coaxial electrode has been carried out by Setiawan and Heister [19]; they compute jet configurations that are driven to pinching in the regime where the electric field enhances the instability. The present study is also in the nonlinear regime but we compute traveling waves of arbitrary amplitude and wavelength.

The full two-dimensional problem involving an electric field has been studied by Papageorgiou and Vanden-Broeck [20,21]. In these papers the authors made no approximations for competing length scales; however,

they neglected the motion of the second bounded fluid. Grandison et al. [22] extended these results to two dimensions by taking into account the motion of the second fluid. In this paper we will extend the results of [20–22] by calculating fully nonlinear three-dimensional axisymmetric flows taking into account capillary forces.

The paper is organized as follows. Section 2 describes the governing equations and gives the exact dimensionless problem for both cases studied. Section 3 presents linearized dispersion relations, again for both cases. Section 4 describes the numerical procedure and in Sect. 5 results are shown for the fully nonlinear scheme along with a comparison between the linear and nonlinear computations. We conclude the paper in Sect. 6.

2 Formulation

In this section we formulate the mathematical models to be addressed for the two cases of a perfectly conducting fluid surrounded by a dielectric gas, and a perfectly conducting annulus with a hollow dielectric core. These models form the basis for the analysis and computations that follow.

2.1 Case 1: Perfectly conducting inner fluid surrounded by a passive dielectric

We consider periodic axisymmetric waves of wavelength λ. The whole flow, which we assume to be stationary with respect to the ground frame, can be decomposed into two separate basic flows. The first one is a uniform cylindrical jet propagating to the right at a constant velocity c. The second flow is a wave riding on the jet and moving to the left with a constant phase velocity c such that the whole flow is stationary (see Figs. 1 and 2). The labels A, B, C and D are used to relate the physical plane to the numerical plane described in Sect. 4 and illustrated in Fig. 3. Here A denotes the position of a peak, B the position of a trough and D the position of the outer electrode. The line $r = r_0$ denotes the position of the solid bottom, which in case 1 will be taken to be $r = 0$.

The fluid is assumed to be inviscid, incompressible; the flow is irrotational and the inner fluid is considered to be a perfect conductor so that the total electric field inside the fluid is zero. Hence, the electric potential throughout the inner fluid is constant (for simplicity taken to be zero) and the interface forms an equipotential surface. A hollow cylindrical electrode having a constant potential V_0, concentric with the flow axis and of radius H, is placed around the whole flow region to provide an electric field.

We introduce cylindrical coordinates r, θ, z. The flow is axisymmetric about the z-axis so that all the variables are independent of θ. We denote by $r = \eta(z)$ the equation of the free surface. We also introduce the velocity potential $\phi(r, z)$, the electric potential $V(r, z)$ and the Stokes stream function $\psi(r, z)$. We choose $z = 0$ at a wave crest and

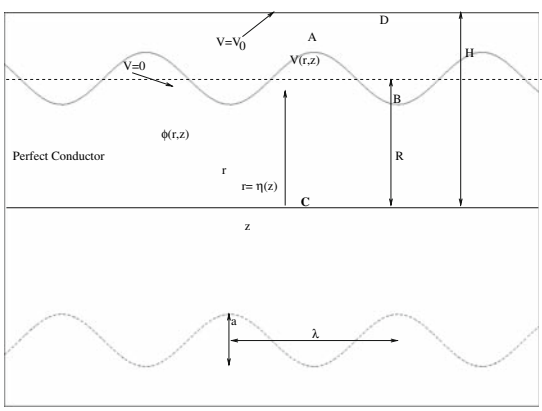

Fig. 1 Diagram showing a typical configuration where the inner fluid is a perfect conductor

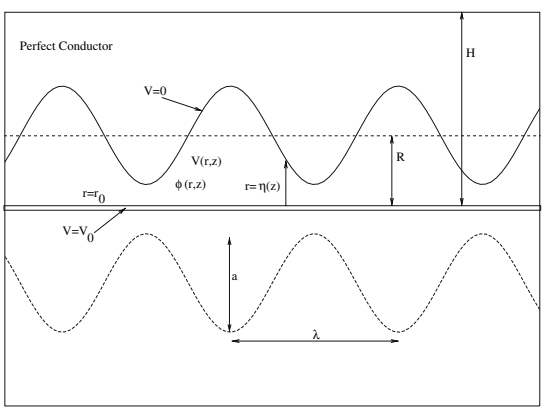

Fig. 2 Diagram showing a typical configuration where the outer fluid is a perfect conductor

also $\phi = 0$ for $0 < r < \eta$ at a wave crest. Also $\psi = 0$ along the z-axis. We denote by Q the constant value of ψ on the free surface. We choose $\phi = \lambda c/2$ at $z = \lambda/2$ for all r where c is the speed of the traveling waves.

The functions ϕ and V satisfy Laplace's equation in cylindrical coordinates,

$$\frac{\partial^2\phi}{\partial r^2} + \frac{1}{r}\frac{\partial\phi}{\partial r} + \frac{\partial^2\phi}{\partial z^2} = 0, \quad 0 < r < \eta(z), \tag{1}$$

$$\frac{\partial^2 V}{\partial r^2} + \frac{1}{r}\frac{\partial V}{\partial r} + \frac{\partial^2 V}{\partial z^2} = 0, \quad \eta(z) < r < H, \tag{2}$$

and the kinematic and dynamic boundary conditions on the free surface which are

$$\phi_r = \phi_z \eta_z, \quad \text{on} \quad r = \eta(z), \tag{3}$$

and

$$\frac{1}{2}(\phi_r^2 + \phi_z^2) - \frac{\sigma}{\rho}K - \frac{P_e}{\rho} = B_0, \quad \text{on} \quad r = \eta(z). \tag{4}$$

Here, K is the curvature of the free surface

$$K = \frac{\eta_{zz}}{(1+\eta_z^2)^{3/2}} - \frac{1}{(1+\eta_z^2)^{1/2}}\frac{1}{\eta}, \tag{5}$$

σ is the surface-tension coefficient assumed to be constant, ρ is the fluid density and B_0 is the Bernoulli constant. The term P_e is the pressure contribution due to the Maxwell stresses induced by the electric field at the interface and is given by

$$P_e = \frac{\varepsilon}{2}E_n^2, \tag{6}$$

where ε is the dielectric permittivity of the outer fluid and E_n denotes the normal component of the electric field at the interface.

Now, the electric boundary condition at the interface requires continuity of the tangential components of the electric field. Since the electric field inside a perfect conductor must vanish, it follows that the tangential electric field at the interface must also vanish. The interface then is an equipotential surface and consequently we obtain

$$\mathbf{E} = -(\nabla\mathbf{V}\cdot\mathbf{n})\mathbf{n}, \tag{7}$$

at the interface, where $\mathbf{n}$ is the outward unit normal directed from the inner towards the outer fluid. We can rewrite the former expression in terms of V and the angle of steepness of the interface, α say, as

$$E_n = \frac{\partial V}{\partial z}\sin\alpha - \frac{\partial V}{\partial r}\cos\alpha, \tag{8}$$

where

$$\tan\alpha = \eta_z. \tag{9}$$

Thus, Bernoulli's equation becomes

$$\frac{1}{2}(\phi_r^2 + \phi_z^2) - \frac{\sigma}{\rho}K - \frac{\varepsilon}{2\rho}\left[\frac{\partial V}{\partial z}\sin\alpha - \frac{\partial V}{\partial r}\cos\alpha\right]^2 = B_0 \quad \text{on} \quad r = \eta(z). \tag{10}$$

The constant B_0 can be found by substituting in (10) the exact solution for a uniform jet $\eta = R$, $V = V_0\log(r/R)/\log(H/R)$ (see (25) below) and $\phi = cz$. The result is

$$B_0 = \frac{1}{2}c^2 + \frac{\sigma}{\rho R} - \frac{\varepsilon}{2\rho}\frac{V_0^2}{(R\log(H/R))^2}. \tag{11}$$

It is useful to define the amplitude of the wave, s, by

$$s = \frac{\eta(0) - \eta(\lambda/2)}{\lambda}, \tag{12}$$

where λ is the wavelength of periodic interfacial waves. This amplitude, s, is used later in our numerical scheme as a parameter. This allows us to define the wave amplitude for which we seek solutions in our fully nonlinear numerical scheme and is particularly important when seeking pinched configurations. We note that the definition of the amplitude (12) is similar to that of the steepness used in two-dimensional wave computations.

Finally we non-dimensionalize our equations by choosing λ as the unit of length, c as the unit velocity and V_0 as the unit of voltage (with this choice we have $V = 1$ on the surface of the hollow electrode). This choice provides unit wavelength but other lengths, such as the radius of the hollow conductor, for example, are scaled accordingly also; to avoid the introduction of additional variables, we will use the same nomenclature as in the dimensional problem, where it is understood that variables are now dimensionless. For example, it should be clear that $r \to r/\lambda$, $z \to z/\lambda$, $H \to H/\lambda$, etc. are dimensionless. This scheme is also used in Sect. 2.2 below, as well as in the remainder of the study. Equations (1)–(2) read the same in dimensionless variables and so does the kinematic condition (3), as well as the expression for the curvature (5).

In terms of the dimensionless variables, the Bernoulli equation (10) becomes

$$\frac{1}{2}(\phi_r^2 + \phi_z^2) - \gamma K - \frac{E_b}{2}\left[\frac{\partial V}{\partial z}\sin\alpha - \frac{\partial V}{\partial r}\cos\alpha\right]^2 = B, \quad \text{on } r = \eta(z), \tag{13}$$

and

$$\gamma = \frac{\sigma}{\rho\lambda c^2}, \quad E_b = \frac{\varepsilon V_0^2}{\rho c^2 \lambda^2}, \quad B = \frac{B_0}{c^2}. \tag{14}$$

The dimensionless parameters γ and E_b represent the ratios of capillary to inertial pressures, and electrical to inertial pressures, respectively (they can be termed inverse Weber and electrical Weber numbers, respectively). This concludes the general formulation of the first problem. For given values of the parameters s, H and E_b we seek γ, B and the functions $\eta(z)$, $\phi(r, z)$ and $V(r, z)$.

2.2 Case 2: Dielectric inner fluid surrounded by a perfectly conducting passive gas

In this case the incompressible inner medium is a dielectric fluid and is bounded by a perfectly conducting hydrodynamically passive medium, e.g., a gas. The electric field inside the inner liquid region is generated by placing a wire electrode of radius $r_0 > 0$ on the axis and connecting it to a constant electric potential source V_0. Since the outer gas medium is a perfect conductor, the electric potential there is a constant which is chosen to be zero. Consequently, both the electric and velocity potentials must be found in the inner region occupied by the dielectric liquid. This is in contrast to case 1 where the potentials ϕ and V must be found inside and outside the interface, respectively.

In what follows, we summarize the basic equations and boundary conditions where non-dimensionalizations have been carried out as explained in Sect. 2.1 above (note that r_0 appearing below is used for the dimensionless quantity r_0/λ). The velocity potential is a harmonic function satisfying

$$\frac{\partial^2\phi}{\partial r^2} + \frac{1}{r}\frac{\partial\phi}{\partial r} + \frac{\partial^2\phi}{\partial z^2} = 0, \quad r_0 < r < \eta(z). \tag{15}$$

The dynamic boundary condition on the free surface becomes,

$$\frac{1}{2}(\phi_r^2 + \phi_z^2) - \gamma K + \frac{E_b}{2}\left[\frac{\partial V}{\partial z}\sin\alpha - \frac{\partial V}{\partial r}\cos\alpha\right]^2 = C, \quad \text{on } r = \eta(z), \tag{16}$$

where

$$C = C_0/c^2, \quad C_0 = \frac{1}{2}c^2 + \frac{\sigma}{\rho R} - \frac{\varepsilon}{2\rho}\frac{V_0^2}{(R\log(r_0/R))^2}, \tag{17}$$

while the kinematic condition reads

$$\phi_r = \phi_z\eta_z \quad \text{on } r = \eta(z). \tag{18}$$

Note the change in sign of the electric pressure term in (16) compared to case 1. This is due to the non-vanishing field in the fluid for case 2 in contrast to case 1. An extra condition in this case is that there is no flow normal to the axial electrode, whence

$$\phi_r = 0 \quad \text{on} \quad r = r_0. \tag{19}$$

The electric potential is also a harmonic function and satisfies

$$\frac{\partial^2 V}{\partial r^2} + \frac{1}{r}\frac{\partial V}{\partial r} + \frac{\partial^2 V}{\partial z^2} = 0, \quad r_0 < r < \eta(z), \tag{20}$$

along with the boundary conditions,

$$V(r_0, z) = 1, \quad V(\eta(z), z) = 0. \tag{21}$$

Note that, since viscosity is absent in our work, the no-slip condition is not relevant.

This concludes the formulation for case 2 and, as with case 1, we seek values for the unknowns γ, C and the functions $\eta(z)$, $\phi(r, z)$ and $V(r, z)$ for the parameters s, Q, r_0 and E_b.

In the next two sections we calculate the position of the free surface for both case 1 and case 2 subject to the boundary values $\psi(r = r_0) = 0$, $\psi(r = \eta) = Q$, $\phi(z = 0) = 0$, $\phi(z = 1/2) = 1/2$.

3 Linear theory

In this section we present a linear theory and derive dispersion relations for each case formulated in Sect. 2 above. We carry out the analysis for the given formulation in order to obtain small-amplitude results that can be compared with the fully nonlinear calculations of Sect. 4.

3.1 Case 1: Perfectly conducting inner fluid surrounded by a passive dielectric

We linearize the dimensionless governing equations and boundary conditions about the exact solution of a uniform cylindrical jet of radius R, writing

$$\eta(z) = R + \tilde{\eta}(z), \tag{22}$$

where here and in what follows tilde quantities are infinitesimally small. Neglecting higher-order terms we obtain the curvature of the perturbed free surface as

$$K = \tilde{\eta}_{zz} + \frac{\tilde{\eta}}{R^2} - \frac{1}{R}. \tag{23}$$

It also follows that the steepness angle α is sufficiently small so that

$$\sin\alpha = \tilde{\eta}_z, \quad \cos\alpha = 1. \tag{24}$$

The velocity and electric potentials are perturbed as follows

$$\phi(r, z) = z + \tilde{\phi}(r, z), \quad V(r, z) = \frac{1}{\log(H/R)}\log(\frac{r}{R}) + \tilde{V}(r, z). \tag{25}$$

The linearized kinematic and dynamic boundary conditions become

$$\tilde{\phi}_r = \tilde{\eta}_z, \quad \text{on} \quad r = R \tag{26}$$

$$\tilde{\phi}_z - \gamma\left[\tilde{\eta}_{zz} + \frac{\tilde{\eta}}{R^2}\right] - E_b f_1 \tilde{V}_r = 0, \quad \text{on} \quad r = R \tag{27}$$

where

$$f_1 = \frac{1}{R\log(H/R)}. \tag{28}$$

The function $\tilde{V}(r,z)$ satisfies the following system

$$\frac{\partial^2\tilde{V}}{\partial r^2}+\frac{1}{r}\frac{\partial\tilde{V}}{\partial r}+\frac{\partial^2\tilde{V}}{\partial z^2}=0,\quad R<r<H, \tag{29}$$

$$\tilde{V}(R,z)=-f_1\,\tilde{\eta}(z), \tag{30}$$

$$\tilde{V}(H,z)=0, \tag{31}$$

and thus the solution has the form

$$\tilde{V}(r,z)=A\left[I_0(kr)-\frac{I_0(kH)}{K_0(kH)}K_0(kr)\right]\cos(kz), \tag{32}$$

where A is an unknown constant, I_0 and K_0 are the modified Bessel functions of the first and second kind, respectively, and k is the dimensionless wavenumber and has the value 2π due to our non-dimensionalization with respect to the wavelength.

The perturbation velocity potential $\tilde{\phi}$ is a harmonic function bounded at $r=0$ and thus we seek a solution of the form

$$\tilde{\phi}(r,z)=DI_0(kr)\sin(kz), \tag{33}$$

where D is an unknown constant. We use (26) and (30) to obtain an expression for $\tilde{\eta}$ and to find D in terms of A. We then substitute the solutions (32)–(33) in the Bernoulli equation (27) to obtain the following dispersion relation in terms of γ,

$$\gamma=\frac{k^2R^2\left[I_0(kR)+E_bf_1^2I_0'(kR)S\right]}{k(k^2R^2-1)I_0'(kR)}, \tag{34}$$

where

$$S=\frac{I_0'(kR)K_0(kH)-I_0(kH)K_0'(kR)}{I_0(kR)K_0(kH)-I_0(kH)K_0(kR)}. \tag{35}$$

We note that in the case where the electric-field term tends to zero ($E_b\to 0$), we recover the dispersion relation of Vanden-Broeck et al. [8]. The result (34) is used later in comparisons with the arbitrary-amplitude computations.

3.2 Case 2: Inner fluid is dielectric and the outer fluid is a conductive gas

In this case, the electric potential $V(r,z)$ at each point $r_0<r<\eta$, $|z|<\infty$, is a harmonic function which vanishes at the perturbed interface $r=R+\tilde{\eta}(z)$ and assumes the value $V=1$ at $r=r_0$; thus it has the form

$$V(r,z)=\frac{1}{\log(r_0/R)}\log(\frac{r}{R})+\tilde{V}(r,z). \tag{36}$$

The perturbation electric potential $\tilde{V}(r,z)$ is also harmonic, vanishes at $r=r_0$, and at the unperturbed interface $r=R$ assumes the value

$$\tilde{V}(R,z)=-\frac{1}{R\log(r_0/R)}\tilde{\eta}(z). \tag{37}$$

This follows by linearization of boundary condition (8).

By applying the above boundary conditions, we obtain the solution

$$\tilde{V}(r,z)=[A_1K_0(kr)+B_1I_0(kr)]\cos(kz), \tag{38}$$

where

$$A_1=-\frac{Ff_2I_0(kr_0)}{I_0(kr_0)K_0(kR)-I_0(kR)K_0(kr_0)},\quad B_1=\frac{Ff_2K_0(kr_0)}{I_0(kr_0)K_0(kR)-I_0(kR)K_0(kr_0)}, \tag{39}$$

and F is an unknown constant, while

$$f_2 = -\frac{1}{R\log(r_0/R)}. \tag{40}$$

The perturbation velocity potential $\tilde{\phi}$ satisfies

$$\frac{\partial^2\tilde{\phi}}{\partial r^2} + \frac{1}{r}\frac{\partial\tilde{\phi}}{\partial r} + \frac{\partial^2\tilde{\phi}}{\partial z^2} = 0, \quad r_0 < r < \eta(z), \tag{41}$$

$$\tilde{\phi}_r(r_0, z) = 0, \tag{42}$$

$$\tilde{\phi}_r(R, z) = \tilde{\eta}_z, \tag{43}$$

where the last condition is the result of linearization of the kinematic condition (3). The solution of the above system is

$$\tilde{\phi}(r, z) = [A_2K_0(kr) + B_2I_0(kr)]\sin(kz), \tag{44}$$

where

$$A_2 = -\frac{FI_0'(kr_0)}{I_0'(kr_0)K_0'(kR) - I_0'(kR)K_0'(kr_0)}, \tag{45}$$

$$B_2 = \frac{FK_0'(kr_0)}{I_0'(kr_0)K_0'(kR) - I_0'(kR)K_0'(kr_0)}. \tag{46}$$

The linearized Bernoulli equation on the unperturbed interface has the same form as in case 1. Thus, using the solutions found above gives the following dispersion relation for case 2

$$\gamma = \frac{k^2R^2}{k(k^2R^2-1)}\left[\frac{I_0(kR)K_0'(kr_0) - I_0'(kr_0)K_0(kR)}{I_0'(kR)K_0'(kr_0) - I_0'(kr_0)K_0'(kR)} + E_bf_2^2\frac{I_0'(kR)K_0(kr_0) - I_0(kr_0)K_0(kR)}{I_0(kr_0)K_0(kR) - I_0(kR)K_0(kr_0)}\right]. \tag{47}$$

4 Numerical scheme

We will now describe the numerical procedure used to solve cases 1 and 2. In both cases we take the velocity potential, ϕ, and the stream function, ψ, as independent variables (see Fig. 3 for a schematic of the computational domain of case 1). In case 1, a second domain is included above and in contact with the (ϕ,ψ)-plane, where Laplace's equation will be solved for the electric potential. The physical domain is mapped as follows: the physical region $0 < z < 1/2$ maps to $0 < \phi < 1/2$ in the lower grid and to $0 < \omega < \omega_{\max}$ in the upper grid where $\omega_{\max}$ is found as part of the solution. The physical range $0 < r < \eta(z)$ maps to $0 < \psi < Q$ and $\eta(z) < r < H$ to $0 < V < V_0$. In case 2 there exists just one computational domain, the $\phi - \psi$ domain of case 1, and all unknowns are found on this single grid; the derivation of the equations used to solve this scheme are discussed in Sect. 4.2.

Following Vanden-Broeck et al. [8] we write the Laplace equation for the fluid dynamics and the corresponding Bernoulli equation in terms of r and its partial derivatives. From [23] we obtain the identities

$$\frac{\partial r}{\partial\phi} = -\frac{1}{J}\frac{\partial\psi}{\partial z}, \quad \frac{\partial r}{\partial\psi} = \frac{1}{J}\frac{\partial\phi}{\partial z}, \tag{48}$$

$$\frac{\partial z}{\partial\phi} = \frac{1}{J}\frac{\partial\psi}{\partial r}, \quad \frac{\partial z}{\partial\psi} = -\frac{1}{J}\frac{\partial\phi}{\partial r}, \tag{49}$$

where J is the Jacobian of the transformation, namely

$$J = \frac{\partial\phi}{\partial z}\frac{\partial\psi}{\partial r} - \frac{\partial\phi}{\partial r}\frac{\partial\psi}{\partial z}. \tag{50}$$

which yields

$$r^3\frac{\partial^2 r}{\partial\psi^2} + r\frac{\partial^2 r}{\partial\phi^2} + r^2\left(\frac{\partial r}{\partial\psi}\right)^2 - \left(\frac{\partial r}{\partial\phi}\right)^2 = 0, \tag{51}$$

$$\frac{1}{2}\left[\left(\frac{\partial r}{\partial \phi}\right)^2 + r^2\left(\frac{\partial r}{\partial \psi}\right)^2\right]^{-1} - \gamma K - \frac{E_b}{2}\left[\frac{\partial V}{\partial z}\sin\alpha - \frac{\partial V}{\partial r}\cos\alpha\right]^2 = B, \tag{52}$$

where

$$K = \frac{\left[r\frac{\partial r}{\partial \psi}\frac{\partial^2 r}{\partial \phi} - \left(\frac{\partial r}{\partial \phi}\right)^2\frac{\partial r}{\partial \psi} - r\frac{\partial r}{\partial \phi}\frac{\partial^2 r}{\partial \phi \partial \psi}\right]}{\left[\left(\frac{\partial r}{\partial \phi}\right)^2 + r^2\left(\frac{\partial r}{\partial \psi}\right)^2\right]^{3/2}} - \frac{\left|\frac{\partial r}{\partial \psi}\right|}{\left[\left(\frac{\partial r}{\partial \phi}\right)^2 + r^2\left(\frac{\partial r}{\partial \psi}\right)^2\right]^{1/2}}, \tag{53}$$

with the boundary conditions

$$r = r_0 \quad \text{on} \quad \psi = 0, \quad 0 < \phi < 1/2, \tag{54}$$

$$\frac{\partial r}{\partial \phi} = 0 \quad \text{on} \quad r_0 < \psi < Q, \quad \phi < \{0, 1/2\}. \tag{55}$$

For case 1 we set $r_0 = 0$. In order to concentrate mesh points about the region where ϕ is most rapidly varying, we introduce the variable t by the transformation

$$\psi = t^2, \tag{56}$$

and using the chain rule we obtain

$$\frac{\partial}{\partial \psi} = \frac{1}{2t}\frac{\partial}{\partial t}, \quad \frac{\partial^2}{\partial \psi^2} = -\frac{1}{4t^3}\frac{\partial}{\partial t} + \frac{1}{4t^2}\frac{\partial^2}{\partial t^2}. \tag{57}$$

We discretize the fluid domain by defining the mesh points

$$\phi_I = \frac{I-1}{2(M-1)}, \quad I = 1, \ldots, M, \tag{58}$$

$$t_J = Q^{1/2}\frac{J-1}{N-1}, \quad J = 1, \ldots, N. \tag{59}$$

For both case 1 and case 2 the governing equations are applied throughout the domain, including at the boundaries $\phi = \{0, 1/2\}$. We evaluate the equations at these boundaries by taking advantage of the wave symmetry at these points to calculate our central finite-difference formulae.

This concludes the portion of the numerical scheme that is common to both cases being investigated. We proceed by outlining the details specific to each case.

4.1 Case 1

For case 1, where the lower fluid is a perfect conductor, we wish to solve Laplace's equation for the incompressible fluid in the lower (ϕ–ψ)-plane and Laplace's equation for the electric field in the upper (ω–V)-plane. The function ω is the conjugate harmonic of the electric potential, V. Therefore ω and V satisfy the Cauchy–Riemann equations $\omega_x = V_y$ and $\omega_y = -V_x$. The computational domain is as indicated in Fig. 3.

First, we obtain an expression similar to Eq. (51) for the electric field in terms of our unknowns r. A fuller discussion on the derivation of such an expression is presented for case 2 in Sect. 4.2 and here we just present the final form of the Laplacian, obtained after some algebra,

$$r^3\frac{\partial^2 r}{\partial \omega^2} - r\frac{\partial^2 r}{\partial V^2} + r^2\left(\frac{\partial r}{\partial \omega}\right)^2 + \left(\frac{\partial r}{\partial V}\right)^2 = 0. \tag{60}$$

In Sect. 4 we described the discretisation used for the lower domain of the problem (the ϕ–ψ-plane). Here in case 1, since the upper fluid is a dielectric, we are required to solve for the electric potential, V, in the upper domain and hence introduce a second discretization for the upper region.

$$\omega_i = \frac{i-1}{2(M-1)}, \qquad i = 1, \ldots, M, \tag{61}$$

$$V_j = V_0 \frac{j-1}{P-1}, \qquad j = 1, \ldots, Q_1. \tag{62}$$

These two grids are coupled at the interface through the dynamic boundary condition.

We now have two instances of Laplace's equation (51) and (60), in terms of the unknowns r, over two different sets of independent variables, ϕ–ψ and ω–V. We satisfy (51) at the mesh points $I = 1, \ldots, M$, $J = 2, \ldots, N-1$ and (60) at the mesh points on the second grid $i = 1, \ldots, M$, $j = 2, \ldots, Q_1 - 1$. An extra M equations are obtained by satisfying (52) at $I = 1, \ldots, M$, $J = N$. At grid points all partial derivatives are calculated using two-point finite-difference formulae for first derivatives and three-point finite-difference formulae for second derivatives. For example

$$\frac{\partial r}{\partial \omega} \approx \frac{r_{i+1,j} - r_{i-1,j}}{2\Delta\omega}$$

$$\frac{\partial^2 r}{\partial \omega^2} \approx \frac{r_{i+1,j} - 2r_{i,j} + r_{i-1,j}}{(\Delta\omega)^2}$$

A final set of three equations is obtained from

$$r_{1,N} - r_{M,N} = s, \tag{63}$$

$$\int_0^{1/2} r \frac{\partial r}{\partial \psi} \mathrm{d}\phi - \frac{1}{2} = 0, \tag{64}$$

$$\int_0^{1/2} r \frac{\partial r}{\partial V} \mathrm{d}\omega - \frac{1}{2} = 0. \tag{65}$$

Equation (63) fixes the amplitude and (64) and (65) fix the wavelength in both the lower and upper regions, respectively. The integrals in (64) and (65) are evaluated by means of the trapezoidal rule.

We calculate the z-coordinates of both the upper and lower grids using the Cauchy–Riemann equations to obtain expressions for ω_z in the upper domain and ϕ_z in the lower domain. This allows us to compute the quantities r at $i = 1, \ldots, M$, $j = 1$ in the upper region 2 by linear interpolation of the points r at $I = 1, \ldots, M$, $J = N$ in the lower region 1. This provides us with $M(N + Q_1 - 3) + 3$ equations. We obtain $M(N + Q_1 - 3) + 3$ unknowns from the $M(N + Q_1 - 3)$ values of r plus γ, B and $\omega_{\max}$. The system of equations was solved by use of a modified Newton iteration scheme. Typical numbers of mesh points used were $M = 20$, $N = Q_1 = 35$ and the mesh was refined further in order to demonstrate that all results presented were independent of the number of mesh points to graphical accuracy.

4.2 Case 2

We begin by writing Laplace's equation for the electric potential V,

$$\frac{\partial^2 V}{\partial r^2} + \frac{1}{r}\frac{\partial V}{\partial r} + \frac{\partial^2 V}{\partial z^2} = 0, \tag{66}$$

in terms of r and its partial derivatives with respect to the independent variables ϕ and ψ.

Using the chain rule we can write the Jacobian, J as

$$J = \left[r \left(\frac{\partial r}{\partial \psi} \right)^2 + \frac{1}{r} \left(\frac{\partial r}{\partial \phi} \right)^2 \right]^{-1}, \tag{67}$$

and its partial derivatives as

$$J_r = \left[\left(\frac{\partial r}{\partial \phi} \right)^2 - \left(\frac{\partial r}{\partial \psi} \right)^2 r^2 \right] \left[\left(\frac{\partial r}{\partial \phi} \right)^2 + \left(\frac{\partial r}{\partial \psi} \right)^2 r^2 \right]^{-2}, \tag{68}$$

$$J_z = -\frac{2r\left(r^2\frac{\partial r}{\partial\psi}\left(\frac{\partial r}{\partial\psi}\right)_z + \frac{\partial r}{\partial\phi}\left(\frac{\partial r}{\partial\phi}\right)_z\right)}{\left[r^2\left(\frac{\partial r}{\partial\psi}\right)^2 + \left(\frac{\partial r}{\partial\phi}\right)^2\right]^2}. \tag{69}$$

The partial derivatives of V become, then,

$$\frac{\partial V}{\partial r} = \frac{J}{r}\frac{\partial r}{\partial\phi}\frac{\partial V}{\partial\phi} + Jr\frac{\partial r}{\partial\psi}\frac{\partial V}{\partial\psi}, \tag{70}$$

$$\frac{\partial^2 V}{\partial r^2} = \left(\frac{\partial\phi}{\partial r}\right)^2\frac{\partial^2 V}{\partial\phi^2} + \frac{\partial V}{\partial\phi}\frac{\partial^2\phi}{\partial r^2} + \left(\frac{\partial\psi}{\partial r}\right)^2\frac{\partial^2 V}{\partial\psi^2} + \frac{\partial V}{\partial\psi}\frac{\partial^2\psi}{\partial r^2}, \tag{71}$$

where

$$\left(\frac{\partial\phi}{\partial r}\right)^2 = \left(\frac{J}{r}\frac{\partial r}{\partial\phi}\right)^2, \tag{72}$$

$$\frac{\partial^2\phi}{\partial r^2} = \frac{\partial J}{\partial r}\frac{1}{r}\frac{\partial r}{\partial\phi} - \frac{J}{r^2}\frac{\partial r}{\partial\phi} + \frac{J}{r}\frac{\partial}{\partial r}\left(\frac{\partial r}{\partial\psi}\right), \tag{73}$$

$$\frac{\partial^2\psi}{\partial r^2} = \frac{\partial J}{\partial r}r\frac{\partial r}{\partial\psi} + J\frac{\partial r}{\partial\psi} + Jr\frac{\partial}{\partial r}\left(\frac{\partial r}{\partial\psi}\right), \tag{74}$$

and finally

$$\frac{\partial^2 V}{\partial z^2} = \left(\frac{\partial\phi}{\partial z}\right)^2\frac{\partial^2 V}{\partial\phi^2} + \frac{\partial V}{\partial\phi}\frac{\partial^2\phi}{\partial z^2} + \left(\frac{\partial\psi}{\partial z}\right)^2\frac{\partial^2 V}{\partial\psi^2} + \frac{\partial V}{\partial\psi}\frac{\partial^2\psi}{\partial z^2}, \tag{75}$$

where

$$\left(\frac{\partial\phi}{\partial z}\right)^2 = \left(J\frac{\partial r}{\partial\psi}\right)^2, \tag{76}$$

$$\frac{\partial^2\phi}{\partial z^2} = \frac{\partial J}{\partial z}\frac{\partial r}{\partial\psi} + J\frac{\partial^2 r}{\partial\phi\partial z}, \tag{77}$$

$$\left(\frac{\partial\psi}{\partial z}\right)^2 = \left(J\frac{\partial r}{\partial\phi}\right)^2, \tag{78}$$

$$\frac{\partial^2\psi}{\partial z^2} = \frac{\partial J}{\partial z}\frac{\partial r}{\partial\phi} + J\frac{\partial^2 r}{\partial\phi\partial z}. \tag{79}$$

This allows us to write Laplace's equation for V entirely in terms of the independent variables ϕ and ψ. For this case we seek our unknown quantities V and r on this same grid. We satisfy (51) and (66) (the latter transformed to the ϕ–ψ plane as described above) at the mesh points $I = 1, \ldots, M$, $J = 2, \ldots, N-1$. An extra $2M$ equations are obtained by satisfying $r = r_0$ at $I = 1, \ldots, M$, $J = 1$ and (52) at $I = 1, \ldots, M$, $J = N$. Two additional equations are obtained from

$$r_{1,1} - r_{N,1} = s, \tag{80}$$

$$\int_0^{1/2} r\frac{\partial r}{\partial\psi}\mathrm{d}\phi - \frac{1}{2} = 0. \tag{81}$$

This gives $2MN + 2(1-M)$ unknowns consisting of the functions r and V at $2(M-2)N$ meshpoints with γ and B providing an extra two unknowns. In order to solve for these unknowns we obtain M equations from the dynamic boundary condition and M equations by fixing the radius of the inner electrode; a further $2M(N-2)$ equations are obtained by solving Laplace's equation for both the velocity and electric potentials in terms of our unknowns and finally two further equations are used to fix the amplitude and the wavelength. This gives a system of $2MN + 2(1-M)$ equations in $2MN + 2(1-M)$ unknowns. The derivatives with respect to ϕ and ψ are found by two-point finite-difference formulae and the system is solved by a modified Newton iteration scheme.

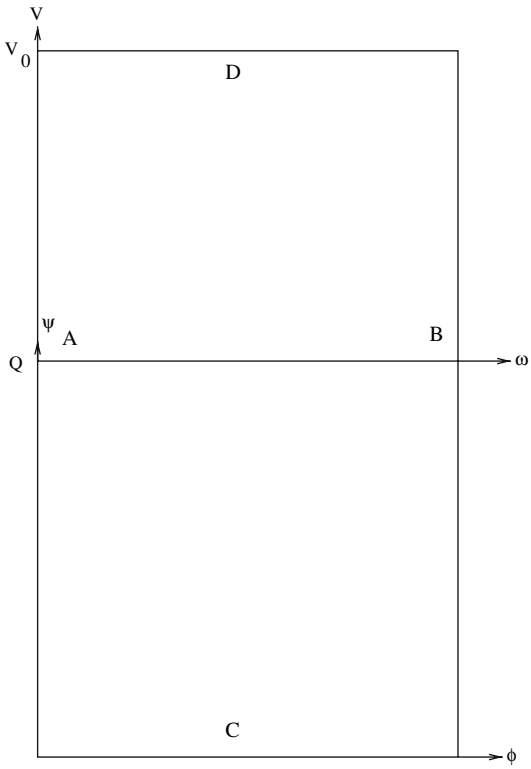

Fig. 3 Schematic of the computational domains in case 1. The lower region is the ϕ–ψ-plane where the fluid dynamics is solved. The upper region is in contact as shown and represents the ω–V-plane, where ω is conjugate harmonic to V

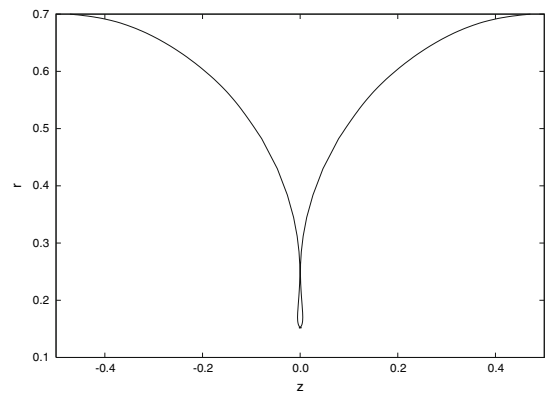

Fig. 4 Free-surface profile in the absence of an electric field, $E_b = 0$; $Q = 1/2\pi^2$, $s = 0.55$, $M = 35$, $N = 50$. The wave contains a trapped bubble at its trough

5 Discussion of results

As a check of the numerical scheme we initially set the electrical parameter $E_b = 0$ in case 1 in order to recover the solutions of Vanden-Broeck et al. [8]. For the parameters used in [8] we find that our numerical scheme is in close agreement with their results. Furthermore, due to increases in computing power (and possibly due to more accurate interpolation formulae) we are able to compute solutions for larger values of the amplitude s, than those in [8]. Figure 4 shows a limiting configuration where the free surface contains a trapped bubble at the trough. We note that, since this flow is axisymmetric, the bubble is toroidal in shape.

5.1 Case 1: results

In this physical situation we have a perfectly conducting inner cylindrical fluid surrounded by a hydrodynamically passive dielectric. Figure 5 shows typical results of two free-surface profiles for two different values of $E_b = 10^{-4}, 0.5$. The amplitude is fixed at $s = 0.6$ in both cases and the radius of the outer electrode is $H = 10$. We note that, in the absence of an electric field, an amplitude of $s = 0.55$ produces a trapped bubble as already shown by the results of Fig. 4. A very small value $E_b = 10^{-4}$, however, shows that a bubble does not form, even at a larger value of the amplitude (dashed line curve). Increasing E_b further to a value of 0.5 indicates a complete disappearance of the bubble (the interfacial shape is now single-valued) associated with a relative reduction in steepness.

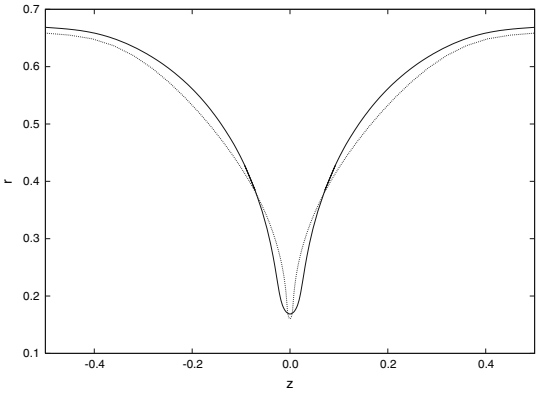

Fig. 5 Case 1. Free-surface profiles for $Q = 1/2\pi^2$, $s = 0.6$, $H = 10$. The dashed curve is the solution for $E_b = 10^{-4}$, and the solid one for $E_b = 0.5$

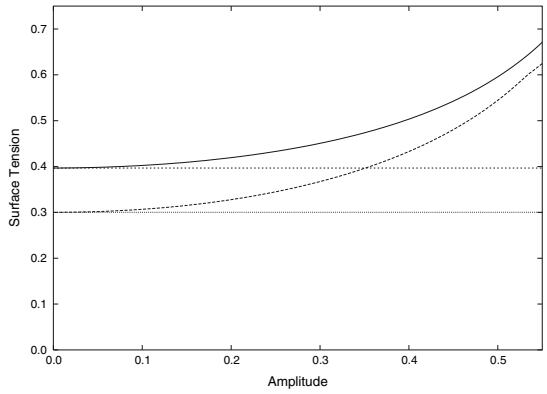

Fig. 6 Case 1. Computed values of the dimensionless surface-tension parameter γ versus amplitude for $Q = 1/2\pi^2$, $H = 10$. The dashed curve represents $E_b = 10^{-6}$, and the solid one $E_b = 0.5$. The horizontal lines represent the corresponding linearized analytic solutions as given by (34)

The variation of the dimensionless surface-tension coefficient γ (see (14)) with wave amplitude is given in Fig. 6 for two different values of $E_b = 10^{-6}, 0.5$. The superimposed horizontal lines correspond to the linear analytic solutions given by the formula (34). Several conclusions are possible from these results. First, an increase in E_b shifts the curve upwards to larger values of γ; this can be deduced analytically in the linear regime from Eq. (34), but the present computations indicate that a monotonic increase of γ with E_b persists at large amplitudes also. The agreement between the full computations and linear theory (the horizontal lines) shows, once again, the accuracy of the present calculations.

5.2 Case 2: results

We now discuss the results for case 2, in which the upper fluid is a perfectly conducting gas and the lower fluid is a dielectric. The dimensionless radius of the inner electrode is set to $r_0 = 0.01$ in all the results that follow. Figure 7 shows the free-surface profiles for $E_b = 0$ and $E_b = 0.05$. Note that the solution in the absence of an electric field is different from the class of solutions computed in [8] due to the presence of the cylindrical rod along the axis of symmetry. This solution is depicted by the dashed curve of Fig. 7. When the electric field is introduced (solid curve), the surface profile becomes more nonlinear and steepens, forming a trapped bubble at its trough. This behavior is qualitatively different from the effect of increasing E_b in case 1 when the inner fluid is a perfect conductor, where we observe a decrease in the wave steepness as E_b increases (see Fig. 5).

Additional nonlinear results are provided in Fig. 8 which depict the variation of γ with wave amplitude at three increasing values of $E_b = 1$, 5 and 10. The analytical linear results given by the dispersion relation (47) are superimposed by straight horizontal lines. We observe, as before, that an increase in E_b at a given amplitude s, results in an increase in γ; this is seen analytically for linear waves from Eq. (47). The variation of γ with amplitude (for a fixed E_b) is not monotonically increasing in case 2 as opposed to case 1, at least for $s \leq 0.5$; see Fig. 6. In fact, there appears to be a maximum of γ at a wave amplitude of approximately 0.43 (the values of s at the maxima for the three different values of E_b are close but unequal). At small amplitudes the numerical scheme shows good agreement with the linear solutions. It can also be seen from Fig. 8 that the range of wave amplitudes where good agreement with linear theory holds, decreases with increasing E_b. For example, linear theory is satisfactory for amplitudes up to about $s = 0.3$ for $E_b = 1$, whereas the corresponding numbers for $E_b = 5$ and 10 are $s \approx 0.1$ and $s = \approx 0.05$, respectively.

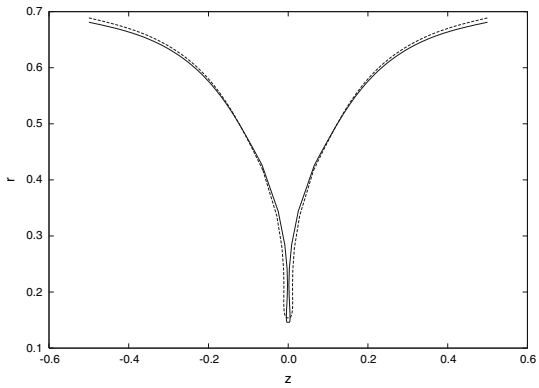

Fig. 7 Case 2. Free-surface profiles for $Q = 1/2\pi^2$, wavelength $\lambda = 1$, amplitude $s = 0.55$, $r_0 = 0.01$. The dashed line represents $E_b = 0$ (not pinched), the solid line represents $E_b = 0.05$ (pinched)

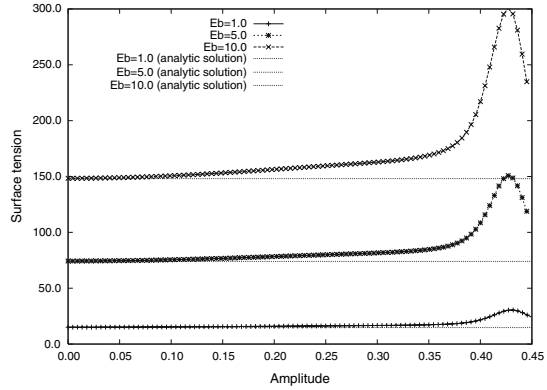

Fig. 8 Case 2. Computed values of γ versus amplitude for $Q = 1/2\pi^2$, $r_0 = 0.01$, $\lambda = 1$ and $E_b = 1$, 5 and 10 as labeled. The horizontal lines represent the corresponding linearized analytic solutions

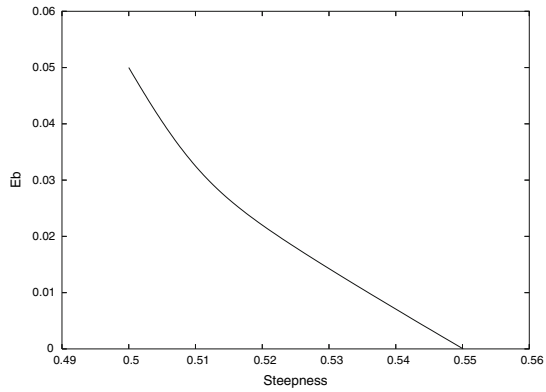

Fig. 9 Computed values of the amplitude required to obtain pinching as a function of E_b for case 2

As the electric field, E_b, is increased the amplitude required to obtain a pinched configuration decreases. Figure 9 shows that the pinching amplitude is a monotonically decreasing function of E_b over the range shown. For the opposite configuration, i.e., where the inner fluid is a perfect conductor and the outer fluid is a dielectric, the interaction of the electric field acts to oppose the formation of a pinch as seen in Fig. 5. Due to the computational complexity of case 1 (two coupled regions), we did not calculate the branch of limiting pinching solutions as was done in Fig. 9 for case 2. As remarked above, we expect an increase of the limiting amplitude with increasing E_b.

6 Conclusions

In this paper we have developed a numerical scheme using finite differences based on the work of Vanden-Broeck et al. [8] and extended their results to take into account the effect of electric fields on the flow.

Two specific electrohydrodynamic problems have been studied, both three-dimensional axisymmetric and driven by radial electric fields. The first (case 1) is concerned with nonlinear traveling waves at the surface of a perfectly conducting liquid jet held at zero potential and surrounded by a coaxial cylindrical electrode held at a constant non-zero potential. The fluid dynamics and the electrostatics must be solved in two different regions. Numerical calculations are presented with particular emphasis placed on limiting waves which overturn to form toroidal bubbles of air inside the fluid. We find that the presence of the field tends to delay the pinching and bubble formation for

waves of equal amplitudes; for example, as seen in Fig. 5 an increase of E_b from 10^{-4} to 0.5 decreases the wave steepness and removes the incipient bubble.

The second problem has a perfectly conducting gas in the annular region surrounding a dielectric fluid which wets axisymmetrically a constant-radius cylindrical-rod electrode placed on the axis and coaxial with the outer electrode. The potential of the outer electrode (and hence the fluid/gas interface) is zero while the rod electrode is kept at a constant non-zero potential. The fluid dynamics and the electrostatics need to be solved in the same region in this case. The effect of the field is qualitatively different in this case as reported in the results of Fig. 7. The trend established numerically is that an increase in the electric-field strength (equivalently an increase in E_b) results in driving equal-amplitude waves to overturning and bubble formation, in direct contrast to the effect of increasing E_b found in case 1. This can be explained by noting that the variation of the surface-tension parameter γ with wave amplitude is different in case 2, where we find an initial increase along with attainment of a maximum followed by a decrease (see Fig. 8 and compare with the analogous one of case 1, Fig. 6). If we slightly increase E_b for a given value of the amplitude in Figs. 6 and 8, then γ increases. However, an increase of γ along the decreasing portions of the curves of Fig. 8 (i.e., to the right of the maxima), corresponds to a decrease in amplitude, in contrast to case 1 which provides an increase in amplitude as seen in Fig. 6. Note that the limiting pinching solutions occur at the largest computed values of the amplitudes in Figs. 6 and 8, and this has guided the discussion of the differences between the two cases above.

We close with a physical argument using a balance of forces that helps to explain the strongly nonlinear wave calculations presented here for cases 1 and 2. As the steepness increases and pinching traveling waves form, there is a competition between capillary forces that tend to increase the wave amplitudes and electric field forces that can either enhance or decrease the capillary mechanism. As can be seen from the Bernoulli equations (13) and (16)—see also [12]—the dimensionless pressure jump, Δp say, according to the normal-stress balance as the interface is crossed from the fluid region is given by $\Delta p_I = (1/R_1 + 1/R_2) - (1/2)\epsilon E_n^2$ for case 1, and by $\Delta p_{II} = (1/R_1 + 1/R_2) + (1/2)\epsilon E_n^2$ for case 2, where $1/R_1$, $1/R_2$ are the principal radii of curvature. Using this force balance, we see that in case 1 the electric field, which is present outside the fluid region, acts to decrease the pressure jump as the interface is crossed from within the fluid in the vicinity of a wave trough; thus, it allows for smaller amplitude, all other effects being equal. In fact, as E_b increases in case 1, the wave amplitudes according to this simple argument are expected to decrease, and this is fully in line with the nonlinear calculations. For case 2, however, the electric field is present in the fluid and is zero outside, which is why the Maxwell stresses act to increase the local pressure jump across the interface as the latter is crossed from inside. This increase in pressure allows for larger amplitudes to form and hence an increase in E_b promotes the formation of a pinch as is seen in our nonlinear computations.

Acknowledgments This work was partially supported by the Engineering and Physical Sciences Research Council, UK, the National Science Foundation Division of Mathematical Sciences and a NATO Collaborative Research Grant.

References

1. Jackson JD (1963) Classical electrodynamics. Wiley, New York
2. Crapper GD (1957) An exact solution for progressive capillary waves of arbitrary amplitude. J Fluid Mech 2:532–540
3. Schwartz LW, Vanden-Broeck JM (1979) Numerical solution of the exact equations for capillary-gravity waves. J Fluid Mech 94:119–139
4. Chen B, Saffman PG (1979) Steady gravity-capillary waves on deep water. Stud Appl Maths 60:183–210
5. Hogan SJ (1980) Some effects of surface tension on steep water waves Part 2. J Fluid Mech 96:417–445
6. Hunter JK, Vanden-Broeck JM (1983) Solitary and periodic gravity-capillary waves of finite amplitude. J Fluid Mech 134:205–219
7. Grandison S, Vanden-Broeck JM (2005) Truncation approximations for gravity-capillary free-surface flows. J Eng Math 54:89–97
8. Vanden-Broeck JM, Miloh T, Spivak B (1998) Axisymmetric capillary waves. Wave Motion 27:245–256
9. Osborne T, Forbes LK (2001) Large amplitude axisymmetric capillary waves. In: King AC, Shikhmurzaev YD (eds) IUTAM symposium on free surface flows. Birmingham, July 2000. Fluid Mechanics and its applications. Kluwer, p 221
10. Burcham CL, Saville DA (2000) The electrohydrodynamic stability of a liquid bridge: Microgravity experiments on a bridge suspended in a dielectric gas. J Fluid Mech 405:37–56

11. Ramos A, Gonzalez H, Castellanos A (1994) Experiments on dielectric liquid bridges subject to axial electric fields. Phys Fluids 6:3206–3208
12. Volkov D, Papageorgiou DT, Petropoulos PG (2005) Accurate and efficient boundary integral methods for electrified liquid bridge problems. SIAM J Sci Comput 26:2102–2132
13. Pelekasis NA, Economou K, Tsamopoulos JA (2001) Linear oscillations and stability of a liquid bridge in an axial electric field. Phys Fluids 13:3564–3581
14. Basset AB (1894) Waves and jets in a viscous liquid. Am J Math 16:93–110
15. Schneider JM, Lindblad NR, Hendricks JrCD, Crawley JM (1967) Stability of an electrified liquid jet. J Appl Phys 38:2599–2605
16. Neukermans J (1973) Stability criteria of an electrified liquid jet. J Appl Phys 44:4769–4770
17. Artana G, Touchard G, Romat H (1997) Absolute and convective instabilities in an electrified jet. J Electrostatics 40–41:33–38
18. Artana G, Romat H, Touchard G (1998) Theoretical analysis of linear stability of electrified jets flowing at high velocity inside a coaxial electrode. J Electrostatics 43:83–100
19. Setiawan ER, Heister SD (1997) Nonlinear modeling of an infinite electrified jet. J Electrostatics 42:243–257
20. Papageorgiou DT, Vanden-Broeck JM (2004) Large-amplitude capillary waves in electrified fluid sheets. J Fluid Mech 508:71–88
21. Papageorgiou DT, Vanden-Broeck JM (2004) Antisymmetric capillary waves in electrified fluid sheets. Eur J Appl Mech 15:609–623
22. Grandison S, Papageorgiou DT, Vanden-Broeck JM (2005) Interfacial capillary waves in the presence of electric fields. European Journal of Mechanics, B Fluids 26:404–421
23. Jeppson RW (1970) Inverse formulation and finite difference solution for flow from a circular orifice. J Fluid Mech 40:215–223